Journal of Materials Chemistry A

ROYAL SOCIETY OF CHEMISTRY

PAPER

View Article Online
View Journal | View Issue

Cite this: J. Mater. Chem. A, 2020, 8, 1394

Facile *in situ* solution synthesis of SnSe/rGO nanocomposites with enhanced thermoelectric performance†

Lisi Huang,‡[a] Jianzhang Lu,‡[a] Duowen Ma,[a] Chunmiao Ma,[a] Bin Zhang,[c] Hengyang Wang,[a] Guoyu Wang,[e] Duncan H. Gregory,[f] Xiaoyuan Zhou*[cd] and Guang Han*[ab]

Constructing nanostructured composite architectures has been considered as an effective strategy to reduce the lattice thermal conductivity (κ_L) and enhance the dimensionless figure of merit (ZT) of thermoelectric materials. Herein, a series of SnSe/reduced graphene oxide (rGO)-x (x = 0.1, 0.3, 0.5, 0.7 wt%) nanocomposites are controllably synthesised *in situ via* a facile single-step bottom-up solution method, where rGO nanosheets are incorporated intimately into the SnSe matrix. Nanocompositing performs two key functions: (i) significantly reducing the lattice thermal conductivity of the material, which can be attributed to enhanced phonon scattering from high-density SnSe/rGO interfaces, and (ii) improving the electrical conductivity over the low temperature range, as result of an increased carrier concentration. The subsequent thermoelectric performance of SnSe/rGO sintered pellets has been optimised by tuning the rGO mass fraction, with SnSe/rGO-0.3 achieving κ_L = 0.36 W m^{-1} K^{-1} at 773 K (cutting the κ_L of SnSe by 33%) to yield a maximum ZT of 0.91 at 823 K (representing a ~47% increase compared to SnSe). This study provides a new pathway to improve the thermoelectric performance of polycrystalline SnSe by way of engineering metal chalcogenide/rGO composite architectures at the nanoscale.

Received 24th October 2019
Accepted 16th December 2019

DOI: 10.1039/c9ta11737g

rsc.li/materials-a

Introduction

The manufacture of disruptive and sustainable energy conversion and storage devices is an important technological response to the global energy crisis. The rational design of new and advanced materials underpins the development of such devices. Thermoelectrics, capable of converting electrical to thermal energy and *vice versa*, offer the prospect of sustainable power generation from waste heat.[1–3] A material's thermoelectric energy conversion efficiency is characterised by its dimensionless figure of merit, $ZT = S^2\sigma T/\kappa$, where S, σ, T and κ represent the Seebeck coefficient, electrical conductivity, absolute temperature and total thermal conductivity (the sum of the electronic and lattice thermal conductivity), respectively.[4,5] Consequently, an effective thermoelectric material should exhibit a large Seebeck coefficient, superior electrical conductivity and low thermal conductivity. However, all these parameters are interdependent, leading to limited possibilities for decoupling them.[6] To date, intensive efforts have been focused on enhancing the power factor, $S^2\sigma$, *via* carrier concentration optimisation,[7–9] resonant doping[10] and band convergence,[11] as well as reducing κ by nanostructuring[12–14] and hierarchical architecturing.[15]

Layered tin selenide (SnSe), with an almost unique combination of Earth-abundant, environmentally compatible elements and outstanding thermoelectric properties, is a standout candidate for mid/high-temperature applications.[16–21] Benefiting from its meagre thermal conductivity, single-crystalline SnSe reached a record-high ZT of 2.6 along the b axis at 923 K.[16] Additionally, the Na-doping of SnSe single crystals delivered a peak ZT of 2.0 (at 773 K) and an exceptional device ZT of 1.34 across a wide temperature range (300–773 K), principally as result of exceptional electronic properties.[17] However, practical application of SnSe is likely to be restricted by the poor mechanical properties of the single crystals. This issue could only be addressed by polycrystalline SnSe if analogous thermoelectric performance can be replicated.[22]

[a]College of Materials Science and Engineering, Chongqing University, Chongqing 400044, China. E-mail: guang.han@cqu.edu.cn

[b]Key Laboratory of Low-grade Energy Utilization Technologies and Systems, Ministry of Education, Chongqing University, Chongqing 400044, China

[c]Analytical and Testing Center, Chongqing University, Chongqing 401331, China. E-mail: xiaoyuan2013@cqu.edu.cn

[d]College of Physics, Chongqing University, Chongqing 401331, China

[e]Chongqing Institute of Green and Intelligent Technology, Chinese Academy of Sciences, Chongqing 400714, China

[f]WestCHEM, School of Chemistry, University of Glasgow, Glasgow, G12 8QQ, UK

† Electronic supplementary information (ESI) available. See DOI: 10.1039/c9ta11737g

‡ These authors contributed equally to this work.

Compositional modification, such as Ag or alkali metal doping[23–25] and creation of Sn vacancies,[26,27] can improve the electronic properties of polycrystalline SnSe and/or reduce its thermal conductivity, but performance has not yet matched that of single crystals.

An alternative approach could be to craft composite or hybrid architectures in which (in)organic secondary structures are integrated with SnSe at the nanoscale. The prospect of "quenching" thermal conductivity at multiple phonon-scattering interfaces and inducing low-energy carrier filtering to raise $S^2\sigma$,[28] is an attractive one and has been implemented in Sb_2Te_3–Pt,[29] Bi_2Te_3–Ag[30] and PbS–Ag composites.[31] Recently, metal chalcogenide/low-dimensional carbon composite materials have demonstrated remarkable thermoelectric properties. For example, Cu_2Se/carbon nanotube (CNT) hybrid materials were prepared by ball milling and sintering, and achieved an exceptional ZT of 2.4 at 1000 K, that could again be attributed to the drop in κ inspired by the introduction of a high density of interfaces.[32] Graphene is hailed as a revolutionary material given its excellent electrical conductivity, large specific surface area, high mechanical strength and ease of functionalisation,[33] making it ideal for energy storage devices, such as Li/Na-ion batteries[34] and supercapacitors.[35] Graphene (and the closely related reduced graphene oxide (rGO)), has also had an immediate impact on the properties of thermoelectrics when introduced to make composites such as $CoSb_3$/rGO,[36] $Ce_{0.85}Fe_3CoSb_{12}$/rGO,[37] PbTe/rGO,[38] Cu_2Se/graphene,[39] and $Cu_{2-x}S$/graphene[40] and when added to conducting polymers.[41,42] The common effect is to reduce κ and/or improve the electronic properties. As such, it is anticipated that forming composites of SnSe and graphene-based materials could be a potent approach to enhance the thermoelectric properties of polycrystalline SnSe. The original precedent for SnSe/rGO materials was in the use of ball milled composites for electrochemical applications,[43] but such a processing approach would likely not be appropriate in facilitating the level of interfacial control at the nanoscale required for thermoelectric applications. In an alternative approach, it was recently demonstrated that SnSe could be incorporated into modified GO matrices, which has profound effects on the thermal and electrical properties of each component.[44]

In this study, we have focused on the role of reduced graphene oxide and its role as an additive rather than as a matrix. The purpose was to assemble nanoinclusions of rGO into well-defined 2D nanosheets of SnSe and to investigate the microstructural effects on the interfacial chemistry and physics as a function of composition systematically. GO possesses hydrophilic functional groups on its surface,[45] allowing efficient dispersion in water and facilitating the formation of homogeneous composites of SnSe and rGO (when reduced from GO). A series of SnSe/rGO-x ($x = 0.1, 0.3, 0.5, 0.7$ wt%) nanocomposites were synthesised *in situ via* a single-step, bottom-up solution method. The processing approach is energy-efficient, scalable to bulk (gram) quantities, uncomplicated and fast. Pellets were spark plasma sintered from the nanocomposite powders and demonstrate both enhanced electrical conductivity (over the low temperature region) and significantly diminished lattice thermal conductivity compared to pellets of SnSe itself. It is possible to optimise the thermoelectric properties by carefully tuning the rGO mass fraction, and pellets of SnSe/rGO-0.3 hit a minimum κ_L value of 0.36 W m^{-1} K^{-1} (773 K) and a maximum ZT of 0.91 (823 K) which is almost 150% of the value obtained for SnSe.

Experimental

Chemicals

$SnCl_2\cdot 2H_2O$ (Aladdin, 99.99%), Se powder (Aladdin, 99.99%), NaOH (Aladdin, 97%), $NaBH_4$ (Alfa, 98%) and graphene oxide (XFNANO, ~99%) were used as supplied.

Materials synthesis and consolidation

SnSe nanomaterials were synthesised and *in situ* combined with various mass fractions (0.1, 0.3, 0.5, 0.7 wt%) of rGO in aqueous solution to form SnSe/rGO nanocomposites. Initially, 100 mmol NaOH, 10 mmol $SnCl_2\cdot 2H_2O$ and an appropriate amount of $NaBH_4$ were dissolved in 40 ml ultrapure water within a three-necked flask to obtain a transparent solution ($NaBH_4$ was utilised in this case to (partially) reduce the graphene oxide that is added in the next step). An ultrasonic homogenous dispersion of graphene oxide (GO) in 10 ml of ultrapure water was added dropwise to the above solution at room temperature while stirring. The aqueous reaction mixture was heated to its boiling temperature using an oil bath. Freshly prepared $NaHSe_{(aq)}$ (50 ml; 0.2 mol l^{-1}) was promptly added to the above boiling solution, boiled for 2 h and cooled to room temperature under Ar (Wangmiao, 99.999%). The products (*ca.* 1.75 g) were collected by centrifuge, washed with ultrapure water and ethanol several times, and dried at 60 °C under vacuum overnight. For comparison, SnSe was prepared by a similar route without the addition of GO. All the samples were stored in an Ar-filled DELLIX glovebox (<0.1 ppm H_2O/O_2) to prevent possible oxidation. SnSe/rGO-x ($x = 0, 0.1, 0.3, 0.5, 0.7$ wt%) powders were compressed by spark plasma sintering (SPS-625) at 550 °C for 5 min into cylindric pellets under vacuum and a uniaxial pressure of ~40 MPa.

Materials characterisation

The phase composition and crystal structures of the samples both in the form of powder and pellet were identified by X-ray diffraction (XRD) using a PANalytical X'pert diffractometer (Cu Kα radiation). Diffraction data were collected from $10 \leq 2\theta/^\circ \leq 80$ with a step size of 0.026° for 10 min. The chemical composition of the solution-synthesised SnSe nanoplates was measured by inductively coupled plasma optical emission spectrometry (ICP-OES, PerkinElmer Optima 8000). The morphology of the samples was characterised by scanning electron microscopy (SEM, Thermo Fisher Scientific Quattro S and JEOL JSM-7800F microscopes, operated at 5 kV). The structural and compositional characteristics were investigated by transmission electron microscopy (TEM, Thermo Fisher Scientific Talos F200S G2, operated at 200 kV). Thin specimens for TEM were prepared from bulk pellets by ion milling (LEICA

EM RES102). Raman spectra were recorded using a HORIBA LabRAM HR Evolution spectrometer with 532 nm laser at room temperature. The oxidation states of Sn, Se and C were analysed by X-ray photoelectron spectroscopy (XPS) (Thermo Fisher Scientific ESCALAB250Xi equipped with monochromatic Al Kα X-ray radiation). The C 1s peak (284.8 eV) was used as the reference to calibrate the binding energies of the other elements' core level spectra. Fourier transform infrared (FTIR) spectra were collected on a Thermo Fisher Scientific Nicolet iS50 spectrophotometer (with a resolution of 4 cm^{-1}) at room temperature.

Thermoelectric performance evaluation

Due to the anisotropic thermoelectric properties of SnSe, the electrical and thermal properties of all the pellets were both measured along the same direction, *i.e.* perpendicular to the pressing direction. The electrical conductivity (σ) and Seebeck coefficient (S) were evaluated using a ULVAC ZEM-3 instrument under He within a temperature range of 300–823 K. The thermal conductivity (κ) was calculated through $\kappa = DC_p\rho$, where D, C_p and ρ represents the thermal diffusivity, heat capacity and density, respectively. The D values of the composite samples were measured using a Netzsch LFA 457 instrument under Ar from 300–823 K. The value of C_p was taken from that reported for SnSe,[16] assuming that the small mass fractions of rGO in the samples would have a negligible effect on the heat capacity. The electronic component of the thermal conductivity, κ_e, was calculated based on the Wiedemann–Franz law (see ref. 46 for details), and the lattice thermal conductivity, κ_L, was then estimated from $\kappa_L = \kappa - \kappa_e$. The density of the SnSe/rGO-x composites was calculated from the respective masses and volumes of the pellets in each case. Finally, the dimensionless figure of merit, ZT, of the composites was calculated through $ZT = S^2\sigma T/\kappa$. Hall measurements were performed to determine the charge carrier density and mobility (Quantum Design DynaCool 9 Physical Property Measurement System, PPMS).

Results and discussion

Fig. 1 shows the XRD patterns for the SnSe/rGO-x ($x = 0$, 0.1, 0.3, 0.5, 0.7 wt%) composites as synthesised through the *in situ* solution method. All the diffraction peaks in each sample pattern can be indexed to orthorhombic SnSe (space group *Pnma*, JCPDS No. 48-1224). Scrutiny of the diffraction patterns reveals no indication of GO or rGO, which is perhaps not unexpected given the low additive content in the synthesised composites. To strengthen this assertion, an SnSe sample with 3 wt% of rGO ("SnSe/rGO-3") was synthesised by the same method, and its XRD pattern (Fig. S1†) reveals a diffraction peak at ~23.6° 2θ that corresponds to (002) plane of rGO,[47] demonstrating the existence of crystalline rGO and the successful reduction of GO as part of the synthetic process.

To confirm the existence of rGO in the composite and understand the degree to which GO was reduced during the *in situ* synthesis, Raman spectra of SnSe, GO and SnSe/rGO-0.3 composite were collected (Fig. 2). The three characteristic peaks

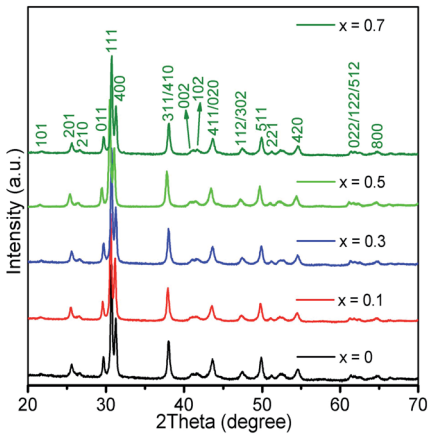

Fig. 1 XRD patterns for the as-synthesised SnSe/rGO-x ($x = 0$, 0.1, 0.3, 0.5, 0.7 wt%) samples.

at around 71.8, 154.5 and 180.1 cm^{-1} in the spectrum of SnSe correspond to the A_g phonon modes, which originate from the planar vibrations of SnSe in the b direction.[48] The peak at ~108.7 cm^{-1} can be assigned to the B_{3g} phonon mode that is derived from the rigid shear modes of SnSe in the c directions.[48] Such peaks are also observed in the spectrum of SnSe/rGO-0.3, although there is a small but discernible red shift, indicating the possible interaction between SnSe and rGO in the composite. The characteristic carbon D (~1350 cm^{-1}) and G bands (~1585 cm^{-1}) appear in the spectrum of SnSe/rGO-0.3, which are related to the vibrations of sp^3-type carbon atoms (typical of disordered, activated carbon) and the sp^2-like carbon atoms typically found in graphitic layers, respectively.[45] It is of interest to note that the intensity ratio of D to G bands increases from 1.56 for GO to 1.67 for SnSe/rGO-0.3, indicating the removal of oxygen-containing function groups (*i.e.* the reduction of GO) and decrease in the average size of the sp^2 domains after GO reduction.[47,49] In addition, the distinct peaks at ~2700 cm^{-1} and ~2900 cm^{-1} refer to 2D and D + G modes in carbon-based materials, respectively.[50] Further evidence of GO reduction could be gleaned from a comparison between the

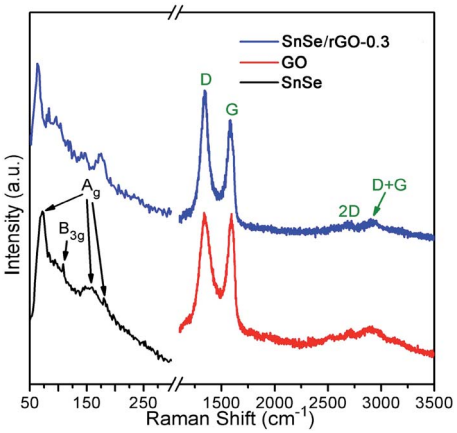

Fig. 2 Raman spectra of SnSe, GO and SnSe/rGO-0.3 composite.

FTIR spectra of GO and SnSe/rGO-0.3 (Fig. S2†). These spectra indicate that the C=O and C–O vibrations diminish considerably in the composite as compared to GO itself.

XPS analysis was performed to investigate the chemical composition of the SnSe/rGO-0.3 surface and to make a comparison with the surface of GO (Fig. 3). The survey scan spectra (Fig. 3a) reveals the presence of Sn, Se, C and O in the composite as compared to C and O only in GO. The C 1s spectrum of GO (Fig. 3b) can be resolved into four peaks at binding energies of 284.8, 286.7, 287.1 and 288.6 eV, assigned to C–C/C=C, C–O, C=O and O–C=O bonds, respectively.[49] These same peaks can be observed in the C 1s spectrum of SnSe/rGO-0.3 at 284.8, 285.9, 287.1 and 289.0 eV, respectively. The strong relative intensity of the C–C/C=C bond peak in the spectrum of the composite contrasts to that of GO, indicating a high degree of GO reduction in the SnSe/rGO-0.3 material.[49] In addition, a peak at ~282.8 eV is also resolved. Previously, such a feature has been attributed to C–Sn bonding in $SnSe_2$/rGO composites,[34] but it is unclear at present as to how such a bonding scheme can be easily rationalised in SnSe/rGO-0.3. The Sn 3d core level (Fig. 3c) can be fitted to two peaks at ~485.9 eV and ~494.3 eV that are assigned to Sn $3d_{5/2}$ and Sn $3d_{3/2}$, respectively, suggesting the divalent nature of the Sn ion.[51] The peaks with slightly higher binding energy of ~487.2 eV and ~495.7 eV correspond to Sn^{4+}, which can be ascribed to surface SnO_2 given the easily oxidizable nature of SnSe[52] and the inevitable contact with air during sample loading. The Se 3d peak (Fig. 3d) can be resolved into two sets of Se $3d_{5/2}$ and Se $3d_{3/2}$ peaks. The binding energy of one set of Se $3d_{5/2}$ and Se $3d_{3/2}$ is centred at 53.9 and 54.8 eV, respectively, suggesting the Se^{2-} valence state.[53] The peaks at higher binding energy of 54.6 eV for Se $3d_{5/2}$ and 55.6 eV for Se $3d_{3/2}$ indicate that the surface Se^{2-} was slightly oxidised, considering the Se $3d_{5/2}$ of Se^0 has a much higher binding energy of ~55.6 eV.[54]

A typical SEM image of the SnSe/rGO-0.3 nanocomposite is presented in Fig. 4a, revealing that fine, thin and wrinkled sheets are embedded within clusters of nanoplates. TEM images (Fig. 4b–d and S3†) show that thin sheets are entwined around the particles (confirmed as SnSe as follows) and are themselves relatively transparent. HRTEM images (for example, Fig. 4e) exhibit a series of lattice fringes with a spacing of 3.0 Å for the nanoplates which corresponds to the {011} planes of SnSe,[55] and a lattice spacing of 3.4 Å for the sheets that is in accordance with the {002} planes of rGO.[45] SnSe nanoplates are "bound" within the rGO sheets. Fig. 4f gives the high angle annular dark field-scanning transmission electron microscopy (HAADF-STEM) image and the corresponding elemental maps of C, Sn and Se. These demonstrate the high homogeneity of the

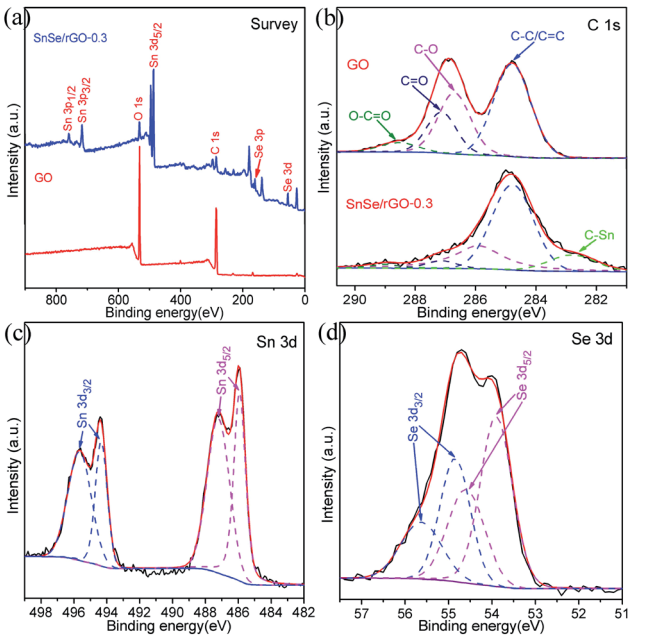

Fig. 3 XPS spectra of GO and SnSe/rGO-0.3 composite: (a) survey scan, (b–d) high-resolution scans for C 1s, Sn 3d and Se 3d, respectively.

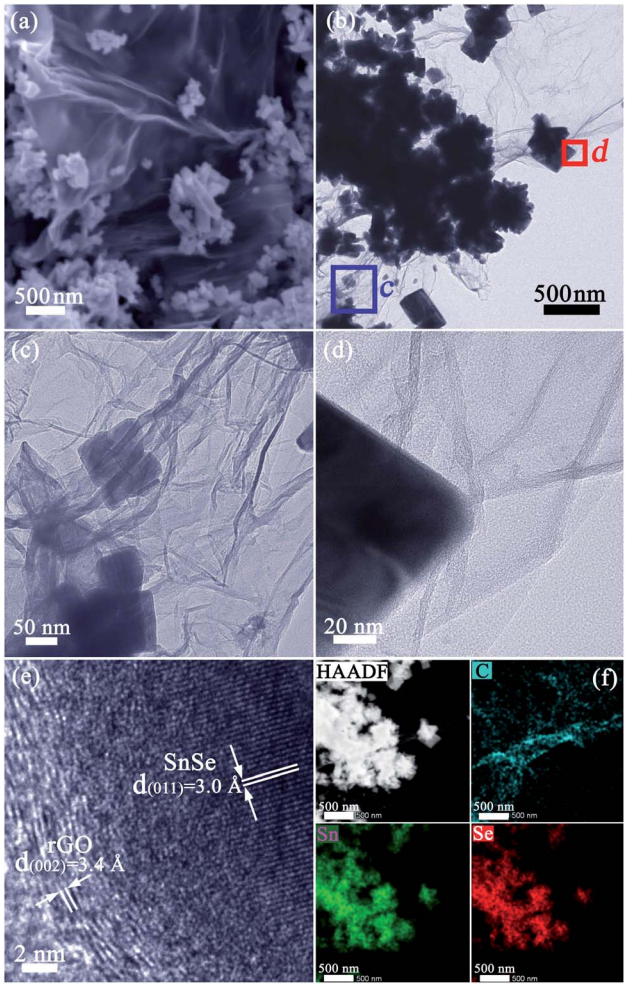

Fig. 4 Electron microscopy characterisation of the SnSe/rGO-0.3 nanocomposite: (a) SEM and (b) TEM images revealing the general morphology, (c and d) higher-magnification TEM images of specific regions marked by a blue square (labelled *c*) and a red square (labelled *d*), respectively in (b), (e) HRTEM image showing the lattice fringes of SnSe and rGO, (f) HAADF-STEM image of the region in (b) and the corresponding elemental maps of C (cyan), Sn (green) and Se (red).

samples, the uniform distribution of Sn and Se within individual SnSe nanostructures, existence of C within thin rGO nanosheets and the co-existence of SnSe and rGO throughout the composite. Additionally, based on HRTEM images of rGO nanosheets aligned parallel to the incident beam direction, the thickness of rGO is estimated to be approximately 3–5 nm.

The as-synthesised SnSe/rGO-x (x = 0, 0.1, 0.3, 0.5, 0.7 wt%) powders were pressed into pellets *via* SPS in order to evaluate their thermoelectric performance. Fig. 5 shows the XRD patterns for the sintered pellets collected along both the parallel and perpendicular to the pressing directions. The diffraction peaks can be indexed exclusively to orthorhombic SnSe (JCPDS No. 48-1224). In addition, the intensities of the (400) peaks are much enhanced in the XRD pattern collected perpendicular to the pressing direction (Fig. 5b), suggesting that strong preferred {h00} orientation occurs in the SnSe pellets.[56,57]

Fig. 6 and S4† show cross-sectional SEM images for SnSe/rGO-x (x = 0, 0.1, 0.3, 0.5, 0.7 wt%) pellets taken perpendicular and parallel to the pressing direction. The microstructures of the pellets are composed of microplates, indicating that solution-synthesised SnSe nanostructures grew further during the high-temperature SPS process. The images illustrate the alignment of the microplates parallel to the pellet surface (Fig. 6c, d and S4d–f†), as manifested in the preferred orientation in XRD patterns (Fig. 5b). Additionally, SEM also reveals that the nanostructure of the rGO was incredibly well preserved in a series of sintered SnSe/rGO-x pellets (*e.g.* x = 0.3, 0.5, 0.7 wt%; insets in Fig. 6d, S4e and f†). The rGO sheets are embedded at various locations among the densely packed SnSe microplates within these composite pellets.

Fig. 7a is a TEM image of a SnSe/rGO-0.3 thinned sample that was prepared from its pellet by ion milling, which unambiguously establishes the two contrasting morphologies of each component; SnSe and rGO. EDS mapping analysis (Fig. 7b) of the region shown in Fig. 7a confirms the co-existence of SnSe plates and rGO nanosheets, as well as providing evidence of the uniform distribution of Sn and Se within the individual SnSe plates (see also Fig. S5†). High magnification TEM images (Fig. 7c, collected from the red inset region in Fig. 7a) further demonstrate the close contact between SnSe plates and the crumpled, almost transparent rGO nanosheets in the composite pellet. An HRTEM image (Fig. 7d, collected from the white inset region in Fig. 7c) reveals the unchanged crystal structure of SnSe after sintering. The SnSe/rGO interfaces in the composite pellets are expected to significantly enhance phonon scattering,

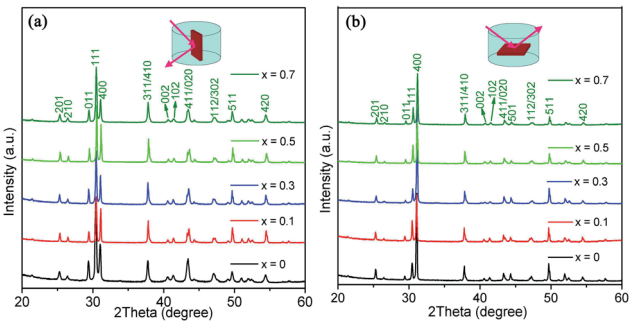

Fig. 5 XRD patterns of SnSe/rGO-x (x = 0, 0.1, 0.3, 0.5, 0.7 wt%) sintered pellets measured (a) parallel and (b) perpendicular to the pressing direction.

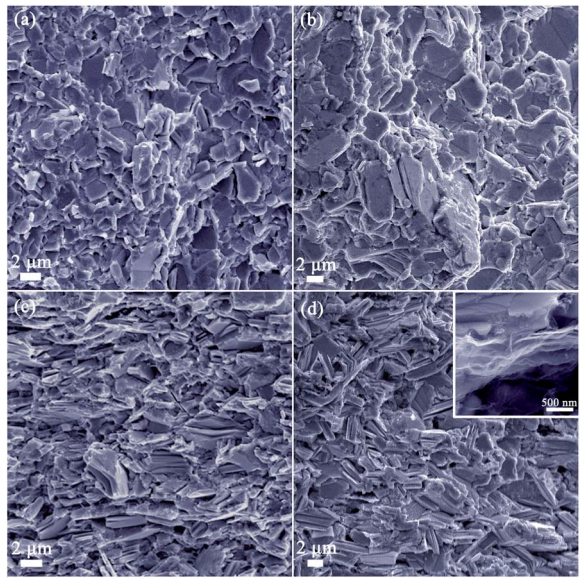

Fig. 6 Cross-sectional SEM images collected from fractured pellets (a and b) perpendicular and (c and d) parallel to the pressing direction for the sintered SnSe/rGO-x pellets: (a and c) x = 0 wt%, (b and d) x = 0.3 wt%. The inset in (d) is a magnified SEM image of part of the SnSe/rGO-0.3 pellet.

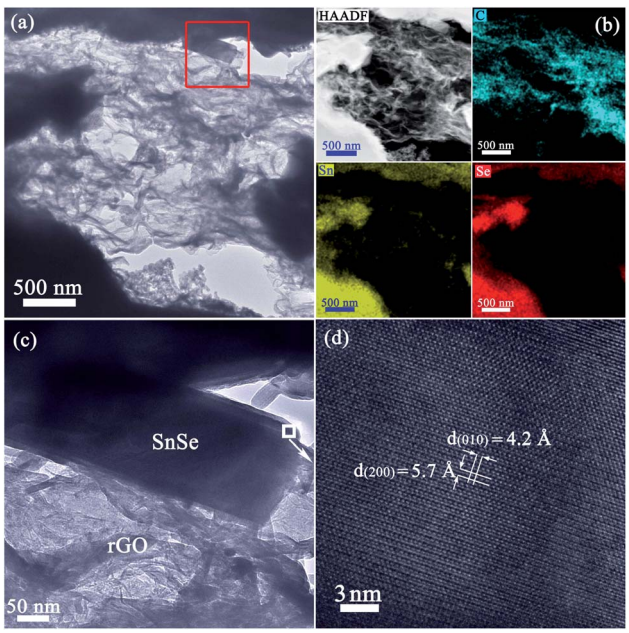

Fig. 7 TEM characterisation of the SnSe/rGO-0.3 pellet: (a) a TEM image of the thinned sample showing the co-existence of SnSe plates and rGO sheets, (b) HAADF-STEM image of the region in (a) and its corresponding element maps of C (cyan), Sn (yellow) and Se (red), (c) a TEM image of region marked by a red square in (a), (d) an HRTEM image of the region marked by a white square in (c).

thus providing a route to reduce the lattice thermal conductivity (as compared to pristine SnSe pellet). This premise was subsequently tested by electrical and thermal property measurements.

Thermoelectric transport properties were measured perpendicular to the pressing direction, as shown in Fig. 8. Fig. 8a presents the electrical conductivity (σ) as a function of temperature for SnSe/rGO-x (x = 0, 0.1, 0.3, 0.5, 0.7 wt%) pellets. For each of the samples, σ initially increases with increasing temperature (up to a temperature of 473–573 K, depending on the mass fraction of rGO), exhibiting semiconducting behaviour. The electrical conductivity then gradually decreases with rising temperature, such that the samples behave more like metals, until a threshold of *ca.* 723 K is reached. Above this temperature, the electrical conductivity once again increases, consistent with the thermal activation of the carriers.[58] Such variations in σ with temperature have been commonly observed in polycrystalline SnSe.[51,56,59,60] All the composite pellets (x > 0) exhibit higher values of σ than that of SnSe over the lower temperature range, while at higher temperature (*e.g.* 773–823 K), the values of σ show less compositional dependence. Interestingly, in the lower temperature region (300–473 K) σ increases monotonically with rGO content, for x = 0.1–0.5, at any given temperature. This increase in σ can be attributed to the increased carrier concentration (n_H) as evidenced from room temperature Hall measurement (Table 1). As has been observed previously, rGO demonstrates p-type conducting behaviour[61] and has been postulated to provide charge carriers to p-type thermoelectric materials, such as $CoSb_3$,[36] $Bi_{0.5}Sb_{1.5}Te_3$ (ref. 62) and $Ce_{0.85}Fe_3CoSb_{12}$,[37] leading to enhanced electrical conductivity in these materials. Addition of rGO may play a similar role in our composites, thus leading to enhanced carrier concentration and electrical conductivity at room temperature. When the rGO mass fraction reaches 0.7 wt%, the room temperature carrier mobility is significantly decreased as compared to SnSe and its composites with lower rGO mass fractions, leading to a decrease in electrical conductivity. This may well be due to enhanced carrier scattering at SnSe/rGO interfaces, which has also been reported in PbTe/rGO,[38] $Bi_{0.5}Sb_{1.5}Te_3$/expanded graphene[62] and $Ce_{0.85}Fe_3CoSb_{12}$/rGO[37] composites.

The temperature dependence of the Seebeck coefficient (S) for all the samples is displayed in Fig. 8b. The positive value of S demonstrates p-type transport behaviour for all compositions and its magnitude first rises with temperature up to 673–723 K and then diminishes (due to bipolar effects) with increasing temperature. Combining the moderate values of S with the relatively high values of σ over the lower temperature range leads to accentuated power factors for the SnSe/rGO composites (Fig. 8c). However, by 823 K the difference between any of the composites and SnSe is not so striking and all the power factor values lie between 0.4 and 0.6 mW m^{-1} K^{-2}.

More extraordinary is the significant reduction in thermal conductivity shown by the nanocomposites. Fig. 8d and e depict the variation in total thermal conductivity (κ_{total}) and lattice thermal conductivity (κ_L) with temperature for all the samples, which first declines to a minimum value at *ca.* 773 K and then increases with temperature (up to the measurement limit of 823 K). This behaviour can be ascribed to a change in the thermal conductivity at the *Pnma–Cmcm* structural phase transition[16] as well as the bipolar effect.[24] In terms of the significance of the rGO content, as x increases from 0 through 0.1 to 0.3 wt%, κ_L dramatically decreases over the whole temperature range. Specifically, the minimum κ_L reached at 773 K is 0.36 W m^{-1} K^{-1} for the SnSe/rGO-0.3 pellet, which is reduced by 1/3 compared to SnSe. The depression in κ_L suggests that a higher density of SnSe/rGO interfaces are responsible for heightened phonon scattering over and above the phonon scattering from the grain boundaries of SnSe itself.[36,38] As x increases further to 0.5 and

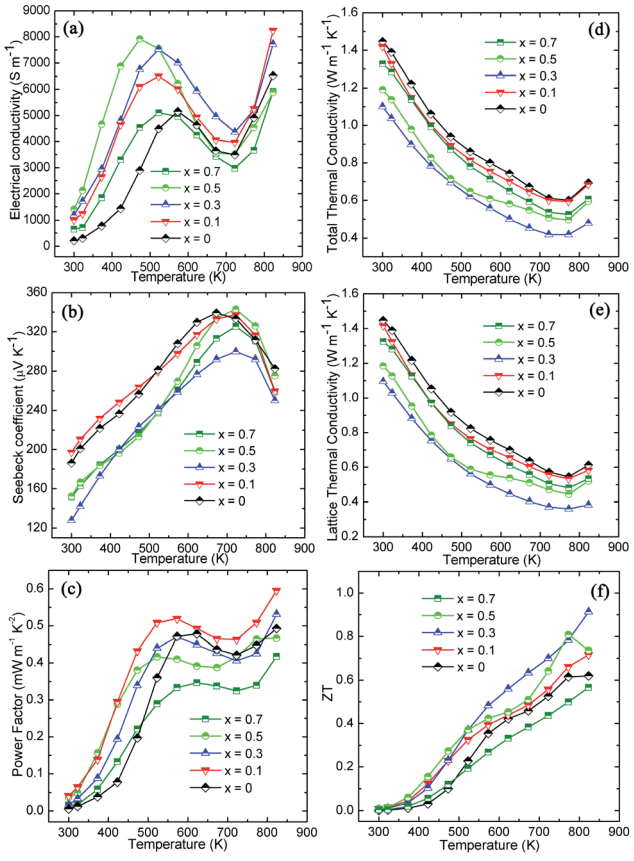

Fig. 8 Temperature-dependant thermoelectric properties of SnSe/rGO-x (x = 0, 0.1, 0.3, 0.5, 0.7 wt%) pellets measured perpendicular to the pressing direction: (a) electrical conductivity, (b) Seebeck coefficient, (c) power factor, (d) total thermal conductivity, (e) lattice thermal conductivity, and (f) the figure of merit, ZT.

Table 1 Electrical conductivity (σ), Hall carrier concentration (n_H) and carrier mobility (μ_H) at room temperature of the SnSe/rGO-x (x = 0, 0.1, 0.3, 0.5, 0.7 wt%) pellets

SnSe/rGO-x pellets	σ [S m^{-1}]	n_H [10^{19} cm^{-3}]	μ_H [cm^2 V^{-1} s^{-1}]
x = 0	208	0.39	3.36
x = 0.1	1005	2.34	2.68
x = 0.3	1182	2.88	2.56
x = 0.5	1405	3.17	2.76
x = 0.7	656	3.05	1.34

0.7 wt% however, κ_{total} and κ_L begin to increase again across the whole temperature range. This behaviour is suggestive that once the rGO concentration reaches a critical value (close to $x = 0.3$ wt%), then the thermal conductivity of the rGO component itself becomes more dominant. Graphene, and to a lesser but still significant extent rGO, possess high thermal conductivity and previous reports also reveal that a high concentration of rGO inclusion increases the thermal conductivity of composite thermoelectrics with the $Yb_yCo_4Sb_{12}$/rGO and ZnO/rGO systems as notable examples.[63,64] Our research reinforces the notion that there is a subtle interplay between interfacial and bulk effects in the rGO component in inorganic/rGO nanocomposites and only at sufficiently low rGO concentration does the interfacial phonon scattering prevail in reducing κ_L.

The variability in the dimensionless figure of merit, *ZT*, as a function of temperature is depicted in Fig. 8f. As compared to SnSe, improved *ZT* values are obtained in the SnSe/rGO-*x* ($x = 0.1$, 0.3, 0.5 wt%) composites over the whole temperature range, whereas the SnSe/rGO-0.7 exhibits *ZT* values that are lower than SnSe at all but the lowest measurement temperatures < 500 K. A peak *ZT* value of 0.91 is obtained at 823 K in the SnSe/rGO-0.3 composite, representing almost 150% of the figure obtained from unmodified SnSe. This *ZT* is superior to many un-doped polycrystalline SnSe prepared by other approaches, such as solvothermal synthesis (*e.g.* ~0.6 (ref. 51) and ~0.8 (ref. 59) at 773 K) and comparable with SnSe prepared *via* zone melting (0.92 at 873 K).[65] Additionally, this *ZT* also compares favourably to that of SnSe/carbon black composites (*ca.* 0.77 at 823 K),[66] and is similar to the maximum value for Na-doped SnSe/CNT composites fabricated by cryogenic grinding and SPS.[67] Considering that the power factors of our samples are still below the optimal values (see ref. 68 for an example), we expect that by combining doping strategies with texture control in optimised SnSe/rGO composites, it should be possible to improve *ZT* values by a considerable margin.

Conclusions

In summary, we have employed a facile and scalable single-step solution-based approach for the bottom-up synthesis of SnSe/rGO nanocomposites *in situ*. Detailed characterisation demonstrates that rGO nanosheets are intimately embedded among a matrix of SnSe nanoplates. The synthesis approach facilitates the control of the rGO concentration in the nanocomposites and introduction of as little as 0.3 wt% rGO results in a significant decrease in the lattice thermal conductivity with the minimum value of 0.36 W m^{-1} K^{-1} at 773 K, representing a ~33% reduction compared to SnSe. This is attributed to a myriad of SnSe/rGO interfaces and SnSe grain boundaries which can effectively scatter phonons. The electrical conductivity over lower temperatures benefits from an increased carrier concentration such that the *ZT* for SnSe/rGO-0.3 peaks at 0.91 (~47% higher than equivalent SnSe samples). This research provides a new perspective in polycrystalline SnSe materials design. This blueprint should be readily extendable to the synthesis of other metal chalcogenide/rGO nanocomposites with similarly tuneable electronic and thermal properties.

Conflicts of interest

There are no conflicts to declare.

Acknowledgements

This work was financially supported by the National Natural Science Foundation of China (No. 51802034, 11674040, 51672270), the Chongqing Research Program of Basic Research and Frontier Technology (No. cstc2018jcyjAX0346), the Chongqing Entrepreneurship and Innovation Program for the Returned Overseas Chinese Scholars (No. cx2018020), the Fundamental Research Funds for the Central Universities (No. 2019CDQYCL003), the Research Funds from Key Laboratory of Low-grade Energy Utilization Technologies and Systems, Ministry of Education, Chongqing University (LLEUTS-201802), the National Training Program of Innovation and Entrepreneurship for Undergraduates (No. 201810611045), and Shenzhen Science and Technology Innovation Committee (JCYJ20170818155752559). DHG acknowledges financial support under the EPSRC grant EP/P510968/1. We would like to thank Guiwen Wang and Xiangnan Gong in Analytical and Testing Centre of Chongqing University for PPMS and Raman measurements, respectively.

References

1 L. D. Zhao, C. Chang, G. J. Tan and M. G. Kanatzidis, *Energy Environ. Sci.*, 2016, **9**, 3044–3060.
2 Z. G. Chen, X. L. Shi, L. D. Zhao and J. Zou, *Prog. Mater. Sci.*, 2018, **97**, 283–346.
3 G. Han, Z.-G. Chen, J. Drennan and J. Zou, *Small*, 2014, **10**, 2747–2765.
4 G. J. Tan, L. D. Zhao and M. G. Kanatzidis, *Chem. Rev.*, 2016, **116**, 12123–12149.
5 S. Ortega, M. Ibanez, Y. Liu, Y. Zhang, M. V. Kovalenko, D. Cadavid and A. Cabot, *Chem. Soc. Rev.*, 2017, **46**, 3510–3528.
6 C. Xiao, Z. Li, K. Li, P. C. Huang and Y. Xie, *Acc. Chem. Res.*, 2014, **47**, 1287–1295.
7 Q. Zhang, E. K. Chere, J. Y. Sun, F. Cao, K. Dahal, S. Chen, G. Chen and Z. F. Ren, *Adv. Energy Mater.*, 2015, **5**, 1500360.
8 Y. B. Luo, Y. Zheng, Z. Z. Luo, S. Q. Hao, C. F. Du, Q. H. Liang, Z. Li, K. A. Khor, K. Hippalgaonkar, J. W. Xu, Q. Y. Yan, C. Wolverton and M. G. Kanatzidis, *Adv. Energy Mater.*, 2018, **8**, 1702167.
9 X. Wang, J. T. Xu, G. Q. Liu, Y. J. Fu, Z. Liu, X. J. Tan, H. Z. Shao, H. C. Jiang, T. Y. Tan and J. Jiang, *Appl. Phys. Lett.*, 2016, **108**, 083902.
10 J. P. Heremans, V. Jovovic, E. S. Toberer, A. Saramat, K. Kurosaki, A. Charoenphakdee, S. Yamanaka and G. J. Snyder, *Science*, 2008, **321**, 554–557.
11 Y. Pei, X. Shi, A. LaLonde, H. Wang, L. Chen and G. J. Snyder, *Nature*, 2011, **473**, 66–69.
12 A. J. Zhang, B. Zhang, W. Lu, D. D. Xie, H. X. Ou, X. D. Han, J. Y. Dai, X. Lu, G. Han, G. Y. Wang and X. Y. Zhou, *Adv. Funct. Mater.*, 2018, **28**, 1705117.

13 G. Han, Z.-G. Chen, L. Yang, M. Hong, J. Drennan and J. Zou, *ACS Appl. Mater. Interfaces*, 2015, **7**, 989–995.
14 S. Chandra and K. Biswas, *J. Am. Chem. Soc.*, 2019, **141**, 6141–6145.
15 K. Biswas, J. Q. He, I. D. Blum, C. I. Wu, T. P. Hogan, D. N. Seidman, V. P. Dravid and M. G. Kanatzidis, *Nature*, 2012, **489**, 414–418.
16 L. D. Zhao, S. H. Lo, Y. S. Zhang, H. Sun, G. J. Tan, C. Uher, C. Wolverton, V. P. Dravid and M. G. Kanatzidis, *Nature*, 2014, **508**, 373–377.
17 L.-D. Zhao, G. Tan, S. Hao, J. He, Y. Pei, H. Chi, H. Wang, S. Gong, H. Xu, V. P. Dravid, C. Uher, G. J. Snyder, C. Wolverton and M. G. Kanatzidis, *Science*, 2015, **351**, 141–144.
18 K. L. Peng, B. Zhang, H. Wu, X. L. Cao, A. Li, D. F. Yang, X. Lu, G. Y. Wang, X. D. Han, C. Uher and X. Y. Zhou, *Mater. Today*, 2018, **21**, 501–507.
19 A. T. Duong, V. Q. Nguyen, G. Duvjir, V. T. Duong, S. Kwon, J. Y. Song, J. K. Lee, J. E. Lee, S. Park, T. Min, J. Lee, J. Kim and S. Cho, *Nat. Commun.*, 2016, **7**, 13713.
20 C. Chang, M. H. Wu, D. S. He, Y. L. Pei, C. F. Wu, X. F. Wu, H. L. Yu, F. Y. Zhu, K. D. Wang, Y. Chen, L. Huang, J. F. Li, J. Q. He and L. D. Zhao, *Science*, 2018, **360**, 778–782.
21 K. Peng, X. Lu, H. Zhan, S. Hui, X. Tang, G. Wang, J. Dai, C. Uher, G. Wang and X. Zhou, *Energy Environ. Sci.*, 2016, **9**, 454–460.
22 S. Sassi, C. Candolfi, J. B. Vaney, V. Ohorodniichuk, P. Masschelein, A. Dauscher and B. Lenoir, *Appl. Phys. Lett.*, 2014, **104**, 212105.
23 C. L. Chen, H. Wang, Y. Y. Chen, T. Day and G. J. Snyder, *J. Mater. Chem. A*, 2014, **2**, 11171–11176.
24 T.-R. Wei, G. Tan, X. Zhang, C.-F. Wu, J.-F. Li, V. P. Dravid, G. J. Snyder and M. G. Kanatzidis, *J. Am. Chem. Soc.*, 2016, **138**, 8875–8882.
25 Z.-H. Ge, D. Song, X. Chong, F. Zheng, L. Jin, X. Qian, L. Zheng, R. E. Dunin-Borkowski, P. Qin, J. Feng and L.-D. Zhao, *J. Am. Chem. Soc.*, 2017, **139**, 9714–9720.
26 W. Wei, C. Chang, T. Yang, J. Z. Liu, H. C. Tang, J. Zhang, Y. S. Li, F. Xu, Z. D. Zhang, J. F. Li and G. D. Tang, *J. Am. Chem. Soc.*, 2018, **140**, 499–505.
27 X. L. Shi, A. Wu, T. L. Feng, K. Zheng, W. D. Liu, Q. Sun, M. Hong, S. T. Pantelides, Z. G. Chen and J. Zou, *Adv. Energy Mater.*, 2019, **9**, 1803242.
28 Y. Zheng, Y. B. Luo, C. F. Du, B. B. Zhu, Q. H. Liang, H. H. Hng, K. Hippalgaonkar, J. W. Xu and Q. Y. Yan, *Mater. Chem. Front.*, 2017, **1**, 2457–2473.
29 D. K. Ko, Y. J. Kang and C. B. Murray, *Nano Lett.*, 2011, **11**, 2841–2844.
30 Q. H. Zhang, X. Ai, L. J. Wang, Y. X. Chang, W. Luo, W. Jiang and L. D. Chen, *Adv. Funct. Mater.*, 2015, **25**, 966–976.
31 M. Ibanez, Z. S. Luo, A. Genc, L. Piveteau, S. Ortega, D. Cadavid, O. Dobrozhan, Y. Liu, M. Nachtegaal, M. Zebarjadi, J. Arbiol, M. V. Kovalenko and A. Cabot, *Nat. Commun.*, 2016, **7**, 10766.
32 R. Nunna, P. F. Qiu, M. J. Yin, H. Y. Chen, R. Hanus, Q. F. Song, T. S. Zhang, M. Y. Chou, M. T. Agne, J. Q. He, G. J. Snyder, X. Shi and L. D. Chen, *Energy Environ. Sci.*, 2017, **10**, 1928–1935.
33 F. Bonaccorso, L. Colombo, G. H. Yu, M. Stoller, V. Tozzini, A. C. Ferrari, R. S. Ruoff and V. Pellegrini, *Science*, 2015, **347**, 1246501.
34 F. Zhang, C. Xia, J. J. Zhu, B. Ahmed, H. F. Liang, D. B. Velusamy, U. Schwingenschlogl and H. N. Alshareef, *Adv. Energy Mater.*, 2016, **6**, 1601188.
35 K. P. Annamalai, L. L. Liu and Y. S. Tao, *J. Mater. Chem. A*, 2017, **5**, 9991–9997.
36 B. Feng, J. Xie, G. S. Cao, T. J. Zhu and X. B. Zhao, *J. Mater. Chem. A*, 2013, **1**, 13111–13119.
37 P. A. Zong, R. Hanus, M. Dylla, Y. S. Tang, J. C. Liao, Q. H. Zhang, G. J. Snyder and L. D. Chen, *Energy Environ. Sci.*, 2017, **10**, 183–191.
38 J. D. Dong, W. Liu, H. Li, X. L. Su, X. F. Tang and C. Uher, *J. Mater. Chem. A*, 2013, **1**, 12503–12511.
39 M. Li, D. L. Cortie, J. X. Liu, D. H. Yu, S. Islam, L. L. Zhao, D. R. G. Mitchell, R. A. Mole, M. B. Cortie, S. X. Dou and X. L. Wang, *Nano Energy*, 2018, **53**, 993–1002.
40 H. C. Tang, F. H. Sun, J. F. Dong, Asfandiyar, H. L. Zhuang, Y. Pan and J. F. Li, *Nano Energy*, 2018, **49**, 267–273.
41 K. L. Xu, G. M. Chen and D. Qiu, *J. Mater. Chem. A*, 2013, **1**, 12395–12399.
42 Z. Zhang, G. M. Chen, H. F. Wang and W. T. Zhai, *J. Mater. Chem. C*, 2015, **3**, 1649–1654.
43 X. Yang, R. Y. Zhang, N. Chen, X. Meng, P. L. Yang, C. Z. Wang, Y. Q. Zhang, Y. J. Wei, G. Chen and F. Du, *Chem.–Eur. J.*, 2016, **22**, 1445–1451.
44 I. S. Protsak, S. Champet, C. Y. Chiang, W. Z. Zhou, S. R. Popuri, J. W. G. Bos, D. K. Misra, Y. M. Morozov and D. H. Gregory, *ACS Omega*, 2019, **4**, 6010–6019.
45 G. X. Wang, J. Yang, J. Park, X. L. Gou, B. Wang, H. Liu and J. Yao, *J. Phys. Chem. C*, 2008, **112**, 8192–8195.
46 L. S. Huang, G. Han, B. Zhang and D. H. Gregory, *J. Mater. Chem. C*, 2019, **7**, 7572–7579.
47 Z. J. Fan, K. Wang, T. Wei, J. Yan, L. P. Song and B. Shao, *Carbon*, 2010, **48**, 1686–1689.
48 Y. J. Huang, L. L. Li, Y. H. Lin and C. W. Nan, *J. Phys. Chem. C*, 2017, **121**, 17530–17537.
49 S. Stankovich, D. A. Dikin, R. D. Piner, K. A. Kohlhaas, A. Kleinhammes, Y. Jia, Y. Wu, S. T. Nguyen and R. S. Ruoff, *Carbon*, 2007, **45**, 1558–1565.
50 C. N. R. Rao, A. K. Sood, K. S. Subrahmanyam and A. Govindaraj, *Angew. Chem., Int. Ed.*, 2009, **48**, 7752–7777.
51 Y. W. Li, F. Li, J. F. Dong, Z. H. Ge, F. Y. Kang, J. Q. He, H. D. Du, B. Li and J. F. Li, *J. Mater. Chem. C*, 2016, **4**, 2047–2055.
52 Y. K. Lee, Z. Luo, S. P. Cho, M. G. Kanatzidis and I. Chung, *Joule*, 2019, **3**, 719–731.
53 G. Han, S. R. Popuri, H. F. Greer, L. F. Llin, J. W. G. Bos, W. Z. Zhou, D. J. Paul, H. Ménard, A. R. Knox, A. Montecucco, J. Siviter, E. A. Man, W.-g. Li, M. C. Paul, M. Gao, T. Sweet, R. Freer, F. Azough, H. Baig, T. K. Mallick and D. H. Gregory, *Adv. Energy Mater.*, 2017, **7**, 1602328.

54 X. M. Zhou, P. Gao, S. C. Sun, D. Bao, Y. Wang, X. B. Li, T. T. Wu, Y. J. Chen and P. P. Yang, *Chem. Mater.*, 2015, **27**, 6730–6736.
55 G. Han, S. R. Popuri, H. F. Greer, J. W. G. Bos, W. Z. Zhou, A. R. Knox, A. Montecucco, J. Siviter, E. A. Man, M. Macauley, D. J. Paul, W. G. Li, M. C. Paul, M. Gao, T. Sweet, R. Freer, F. Azough, H. Baig, N. Sellami, T. K. Mallick and D. H. Gregory, *Angew. Chem., Int. Ed.*, 2016, **55**, 6433–6437.
56 S. J. Liang, J. T. Xu, J. G. Noudem, H. X. Wang, X. J. Tan, G. Q. Liu, H. Z. Shao, B. Yu, S. Yue and J. Jiang, *J. Mater. Chem. A*, 2018, **6**, 23730–23735.
57 J. H. Zhang, J. T. Xu, X. J. Tan, H. X. Wang, G. Q. Liu, H. Z. Shao, B. Yu, S. Yue and J. Jiang, *J. Mater. Chem. C*, 2019, **7**, 2653–2658.
58 X. L. Shi, K. Zheng, M. Hong, W. D. Liu, R. Moshwan, Y. Wang, X. L. Qu, Z. G. Chen and J. Zou, *Chem. Sci.*, 2018, **9**, 7376–7389.
59 D. Feng, Z.-H. Ge, D. Wu, Y.-X. Chen, T. Wu, J. Li and J. He, *Phys. Chem. Chem. Phys.*, 2016, **18**, 31821–31827.
60 G. Han, S. R. Popuri, H. F. Greer, R. Z. Zhang, L. Ferre-Llin, J. W. G. Bos, W. Z. Zhou, M. J. Reece, D. J. Paul, A. R. Knox and D. H. Gregory, *Chem. Sci.*, 2018, **9**, 3828–3836.
61 N. Xiao, X. C. Dong, L. Song, D. Y. Liu, Y. Tay, S. X. Wu, L. J. Li, Y. Zhao, T. Yu, H. Zhang, W. Huang, H. H. Hng, P. M. Ajayan and Q. Y. Yan, *ACS Nano*, 2011, **5**, 2749–2755.
62 D. Suh, S. Lee, H. Mun, S. H. Park, K. H. Lee, S. W. Kim, J. Y. Choi and S. Baik, *Nano Energy*, 2015, **13**, 67–76.
63 P. A. Zong, X. H. Chen, Y. W. Zhu, Z. W. Liu, Y. Zeng and L. D. Chen, *J. Mater. Chem. A*, 2015, **3**, 8643–8649.
64 D. S. Chen, Y. Zhao, Y. N. Chen, B. A. Wang, H. Y. Chen, J. Zhou and Z. Q. Liang, *ACS Appl. Mater. Interfaces*, 2015, **7**, 3224–3230.
65 Y. Fu, J. Xu, G.-Q. Liu, J. Yang, X. Tan, Z. Liu, H. Qin, H. Shao, H. Jiang, B. Liang and J. Jiang, *J. Mater. Chem. C*, 2016, **4**, 1201–1207.
66 J. C. Li, D. Li, W. Xu, X. Y. Qin, Y. Y. Li and J. Zhang, *Appl. Phys. Lett.*, 2016, **109**, 4.
67 F. Chu, Q. H. Zhang, Z. X. Zhou, D. K. Hou, L. J. Wang and W. Jiang, *J. Alloys Compd.*, 2018, **741**, 756–764.
68 X. Wang, J. T. Xu, G. Q. Liu, X. J. Tan, D. B. Li, H. Z. Shao, T. Y. Tan and J. Jiang, *NPG Asia Mater.*, 2017, **9**, e426.